# Soft Matter

Accepted Manuscript

This is an *Accepted Manuscript*, which has been through the Royal Society of Chemistry peer review process and has been accepted for publication.

Accepted Manuscripts are published online shortly after acceptance, before technical editing, formatting and proof reading. Using this free service, authors can make their results available to the community, in citable form, before we publish the edited article. We will replace this *Accepted Manuscript* with the edited and formatted *Advance Article* as soon as it is available.

You can find more information about *Accepted Manuscripts* in the **Information for Authors**.

ROYAL SOCIETY OF CHEMISTRY

www.rsc.org/softmatter
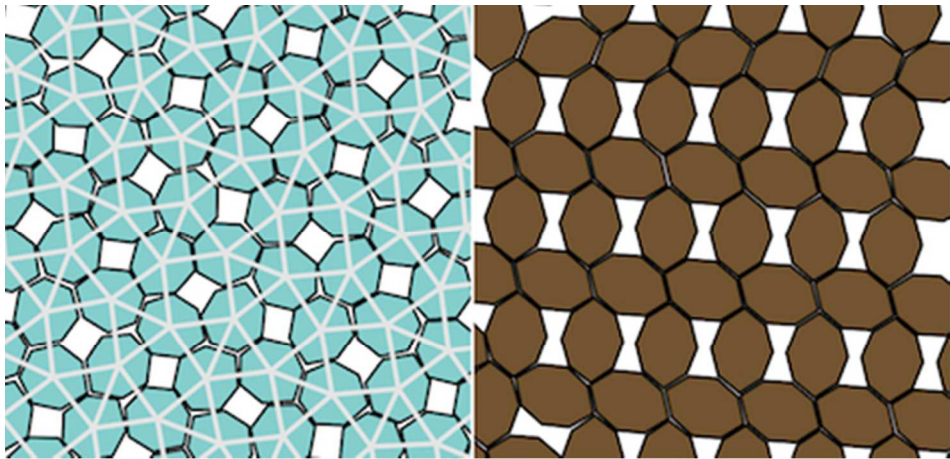
Effect of Shape on the Self-Assembly of Faceted Patchy Nanoplates with Irregular Shape into Tiling Patterns

Jaime A. Millan[†a], Daniel Ortiz[†b], Sharon C. Glotzer*[a,b]

[a]Department of Materials Science and Engineering, University of Michigan, Ann Arbor, MI 48109, USA

[b]Department of Chemical Engineering, University of Michigan, Ann Arbor, MI 48109, USA, E-mail:

sglotzer@umich.edu; Tel : 1 + 734 615 6296

Abstract: Recent reports of the synthesis and assembly of faceted nanoplates with a wide range of shapes and composition motivates the possibility of a new class of two-dimensional materials with specific patterns targeted for a host of exciting properties. Yet, studies of how nanoplate shape controls their assembly – knowledge necessary for their inverse design from target structures – has been performed for only a handful of systems. By constructing a general framework in which many known faceted nanoplates may be described in terms of four anisotropy dimensions, we discover design rules to guide future synthesis and assembly. We study via Monte Carlo simulations attractive polygons whose shape is altered systematically under the following four transformations: faceting, pinching, elongation and truncation. We report that (i) faceting leads to regular porous structures (ii) pinching stabilizes complex structures such as dodecagonal quasicrystals (iii) elongation leads to asymmetric phase behavior, where low and high aspect ratio nanoplates self-assemble completely different structures and (iv) low and high degrees of truncation transform a complex self-assembler into a disk-like assembler, providing design ideas that could lead to switchable structures. We provide

important insight into how the shape and attractive interactions of a nanoplate can be exploited or designed to target specific classes of structures, including space-filling, porous, and complex tilings.

1.   Introduction

Particle shape can influence profoundly the catalytic,[1] plasmonic,[2,3] photonic[4] and mechanical[5] properties of complex crystal structures.[6] In particular, nanoplates[7–9] - nanocrystal with lateral dimensions that are approximately an order of magnitude larger than one specific orthogonal dimension or thickness - have excellent catalytic,[10] optical,[11] and antibacterial[12] properties. Two-dimensional assemblies of perovskites, such as $PbTiO_3$,[13] have interesting ferroelectric and storage properties.[14] Truncation can alter the plasmon resonance of silver nanomaterials by red-shifting the extinction spectra.[3] Truncated nanoplates of single crystal berzelianite can alter the near-infrared band optical absorption properties of this nonstoichiometric semiconductor.[14] By controlling the shapes of nanoplates, targeted and tunable properties should be possible.

  For a range of materials, nanoplate shape emerges during the growth process in others, shapes below several microns (i.e. within the Brownian limit) may be molded, printed, or otherwise obtained. One may envision that nanoplates may attain different shapes through either "passive" or "active" means. By *passive* we refer to transformations made from one system to another during synthesis, as in the case of parallel studies of two related shapes, but not in the context of a single experiment or during the assembly process.[15–18] By *active* we refer to *in situ* morphing, or shape-shifting, of nanoplates among multiple shapes.[19-22] In this work we focused on the *passive* case, where one considers which of many possible synthesizable shapes to make in order to obtain a desired target structure. In both scenarios, a fundamental understanding of the relationship between nanoplate shape, the thermodynamically preferred state of a system of nanoplates, and the kinetic accessibility of those states, is desired.

We consider four shape-related anisotropy dimensions[23] along which systematic shape transformations are possible for facetted, convex nanoplates: faceting, pinching, elongation (aspect ratio) and truncation. All four are shown applied to polygons in Fig. 1. Faceting, elongation, and truncation (of vertices) are self-explanatory. Pinching is a symmetry-breaking transformation that converts a regular polygon into an irregular one (see Fig. S2). All four shape transformations alter the directional entropic[24] and enthalpic[25] forces between nanoplates by altering one or more edge lengths. Fig. 1 shows example experimental manifestations of these four transformations taken from the literature. Gold provides an example of the faceting transformation because it can form triangular, square, pentagonal, hexagonal, nonagonal, and dodecagonal nanoplates and microplates.[26,27] The pinch transformation is observed in silver nanorods that grow into triangular nanoflags.[28] Uranium oxide hydroxide and gold both can form hexagonal and elongated hexagonal nanoplates, demonstrating a passive elongation transformation.[25,29,30,31] Gold and silver nanoplates provide examples of truncation gold forms triangular, truncated triangular, and hexagonal nanoplates,[32] and silver nanoplates can actively transform between triangular and hexagonal nanoplates via truncation under UV irradiation.[33]

Shape transformations in nanocrystal formed from different materials can lead to the introduction or suppression of different types of interaction forces comparable to thermal energies and thus crucial during self-assembly. For example, for a specific amount truncation, CdTe truncated tetrahedra exhibit a permanent dipole that act as one of the driving forces behind the formation of free-floating nanosheets.[34] Highly elongated CdSe nanorods also show electrostatic dipoles that scales linerarly with the volume of the nanorod. [35,36] Near field forces can also be introduced with external electric fields and can either red-shift or blue-shift the surface plasmon resonance of two-dimensional silver[37] or gold[38] nanoparticle arrangements with varying interparticle distance. However, for a systematic and extensive study on the effect of shape, we assume that shape-induced entropic and ligand-induced attractive forces mainly govern the self-organization process of nanoplates.

Here we investigate the pinch, elongation, and truncation shape transformations applied to the family of regular n-sided regular polygons (n-gons) (i.e. the faceting dimension) to understand the role of shape on nanoplate assembly. First, we establish that – with the exception of the regular pentagon, heptagon and octagon – the regular n-gons self-assemble into Archimedean tilings. We then systematically transform each regular n-gon using the pinch, elongation or truncation transformations. The effect of each transformation on self-assembly is categorized to identify commonalities and trends. This library of shape transformations serves to guide the development of a design framework to improve the assembly properties of a faceted nanoplate.

2.   Model and Method

Each nanoplate is modeled as a mathematically hard polygon with short-ranged attractive patches on each edge. In the vicinity of two nanoplates, a pair of edges each with characteristic lengths l_1 and l_2 ($l_1 \geq l_2$) interacts via a pair potential that depends on three independent parameters (see Supplementary Fig. 1): relative orientation angle θ, parallel shift $d_{\parallel}$, and normal distance $d_{\perp}$. The potential energy can then be written as a product of independent terms so that $V(\theta, d_{\parallel}, d_{\perp}) = -\epsilon V(\theta)V(d_{\parallel})V(d_{\perp})$ with attraction strength $\epsilon > 0$, where

$$V(\theta) = 1 - \left(\frac{1 - \cos(\theta)}{1 - \cos(\theta_0)} \right)^2 ,$$

$$V(d_{\parallel}) = \begin{cases} l_2, & \text{if } d_{\parallel} \leq (l_1 - l_2)/2, \\ (l_1 + l_2)/2 - d_{\parallel}, & \text{if } d_{\parallel} > (l_1 - l_2)/2, \end{cases}$$

$$V(d_{\perp}) = 1 - (1 - d_{\perp}/d_0)^2 ,$$

for $\cos(\theta) < \cos(\theta_0) = 0.95$, $d_{\parallel} < (l_1 + l_2)/2$, $d_{\perp} < 2d_0 = 0.4\, l_1$ and 0 otherwise. The attractive strength is set equal to $\epsilon = 1\, k_B T$ for each patch. The geometric constraint $\cos(\theta) < \cos(\theta_0) = 0.95$ enforces the interaction between a misoriented pair of edges to vanish in the limit of multiple edges allowing for a finite convergence in the energy calculations per particle. The edge-edge interaction potential can be

4

decomposed into three components: parallel, perpendicular, and angular (Fig. S1). Each component of the interaction potential models, in a minimal way, different aspects of the ligand-induced van der Waals, solvophobic or other attractive interactions (e.g. DNA linkers) that may be present between nanoparticles.[33] The perpendicular component ($V(d_{\parallel})$) is chosen to be strongest at twice the length of ligand stabilizers, while the parallel ($V(d_{\perp})$) and angular ($V(\theta)$) components model the contact area and steric repulsion between ligands. Assuming ligand-ligand attractive forces dominate over other type of forces (electrostatic or magnetic forces), we scale the angular and distance cutoff based on the length of the ligands. The angular and perpendicular components scale quadratically with separation distance and relative misalignment between adjacent edges, and the parallel component scales linearly with the amount of edge-to-edge contact (Fig. S1). The overall attraction is maximized when the edges are aligned, centered, and almost in contact. The simplified model we used does not include thermodynamic effects such as ligand reorganization (e.g. bundling or ligand crystallization) or explicit solvent effects during the self-assembly process. Instead, it provides a "zeroth" order modeling of nanoplate-nanoplate interactions based on net attraction and particle shape.

Monte Carlo (MC) simulations in the NVT ensemble are used to find equilibrium assemblies from a given set of identical nanoplates. Simulations of attractive systems were only performed at intermediate densities to be in accordance with experimental protocols as in Ref (25). We use the NVT ensemble to simulate at fixed target density. We selected the Monte Carlo method as our approach because it allows us to easily include the shape of the particles and quickly reach equilibrium. For our systems, we find NVT simulations to be faster than NVT than NPT simulations, as it is usually the case. We expect other methods, which exactly capture the particle shape to reach equilibrium structures under the same thermodynamic conditions. MC moves consisted of random rotational or translational moves applied to each nanoplate that are accepted if no overlap is observed or rejected otherwise. Overlap checks are performed using the GJK algorithm as in Ref (25). System sizes range from 800 to 2000 particles. For each state point ten independent of 10^7 MC steps starting from different random configurations were performed to the s equilibration of structures by implementing established simulation codes.[1,25] For each case, statistically identical structures were obtained.

3.   Results and discussion

We present the results for the four shape transformations – faceting, pinching, elongation and truncation – applied to each member of the *n*-gon, for *n* = 1-12 at intermediate densities (packing fraction values between 0.5 and 0.7). For the faceting transformation, we also studied the cases *n* = 13-16 to find the limiting n_o to find the limiting disk-like behavior of the polygons. To fully elucidate the phase diagrams for the pinching, elongation and truncation transformations, we quantify each transformation with geometric parameters that range from 0 to 1 and explored these ranges by applying 0.1 increments on each characteristic geometric factor. In most cases we obtain ordered crystals after proper annealing and snapshots of structures that deviate from those formed from regular polygons are shown in Figs 3-5. For any particular system, changes in interaction strength (ϵ) led to the same final structure and only affected the thermodynamic properties by rescaling the assembly temperature. Each structure is identified by its crystallographic bond network drawn from the centers of the nanoplates.

3.1. Faceting

The faceting transformation alters the number of edges of a regular polygonal nanoplate within a given *n*-gon family (Fig. 2a). Overall, we find the effect of faceting on self-assembly can be divided into three cases at intermediate densities: (i) Archimedean tilings results only for *n* = 3, 4, 6, 8 and 12 (Archimedean tilings are edge-to-edge tilings of regular tiles with group symmetries that act transitively on incident vertex, edges and tiles). (ii) Frustrated assemblies (structures with no global order that show competing local motifs) result at intermediate *n* for some odd number vertices (*n* = 5, 7, 9 and 14). (iii) Effective "rounding" of the nanoplates for *n* > 9 produces assemblies expected from attractive, disk-like particles.

   Members of the *n*-gon family self-assemble into ordered structures identical to an Archimedean tiling when polygons and "gaps" are viewed as independent tiles. For a subset of these polygons, the

densest packings are identical to the assembled tilings. It is known that polygons tend to form dense periodic packings with quasi 6-fold symmetry.[39] In those tilings, the packing's contact types are either edge-to-edge or a combination of both edge-to-edge and edge-to-vertex for polygons with even or odd numbers of vertices.[39] Regular polygons with assemblies in the Archimedean tiling class include the regular triangle, square, hexagon, octagon, and dodecagon these self-assemble the (3^6), (4^4), (6^3), (4.8^2), and (3.12^2) Archimedean tilings, respectively (Fig. 2b, c, e, g and k). Our previous work on the self-assembly of the Archimedean tilings shows that the (3^6), (4^4), (6^3), and (3.12^2) tiling can also self-assemble without attraction between the nanoplates and due solely to entropy, whereas the (4.8^2) Archimedean tiling requires enthalpic patches.[40]

The regular pentagon, heptagon, and nonagon (See Fig. 2d, f and h) do not form ordered assemblies on the time scale of our simulations. These polygons have five-fold, seven-fold, and nine-fold rotational symmetry, respectively, rendering them inconsistent with the standard Bravais lattice coordination. Theoretical work on the five- and seven-fold coordinated nearest-neighbor defects indicate increased frustration and crystallization inhibition.[41] Experimental work on the assembly of five-fold symmetric hydrocarbons has shown glass formation.[42] Liquid crystals can form five-fold, seven-fold, and nine-fold quasicrystals.[43] This propensity in nature for five-, seven-, and nine-fold symmetric entities to self-assemble disordered and/or quasicrystal structures argues for frustration and competition to be prevalent in the assembly of pentagons, heptagons, and nonagons, and this is indeed what we observe.

The more vertices a polygon has, the more the shape approximates that of a disk. At small $n < 9$, n-gons that do assemble into space filling structures exhibit a density-driven transition upon compression at constant temperature from the previously discussed structures (at intermediate densities) to the densest packing structures. For example, a phase transition between the (4.8^2) Archimedean tiling and the (3^6) packing occurs at high packing fraction for the regular octagon. For $n > 9$, the assemblies resemble the expected assembly for hard disks. The regular decagon assembles the (3^6) tiling at higher density but a rhombic crystal at lower density (see Fig. 2i and m). The undecagons,

tridecagons and hexadecagons each form a sheared (3^2.4.3.4) Archimedean tiling (Fig. 2f, k and o), also known as the snub square (SS) tiling or sigma phase, a periodic approximant of a 12-fold quasicrystal. Tetradecagons form center rectangular lattices and pentadecagons formed a disordered structure with no global order (Fig. 2n). A transformation between the sheared (3^2.4.3.4) Archimedean tiling to the (3^6) Archimedean disk tiling occurs for $n \geq 17$.

3.2. Pinching

The pinch transformation alters the geometry of an *n*-gon by moving a vertex radially from the center. We investigate the pinch transformation while preserving the convexity of the building block. Pinching transforms a regular polygon with *n* vertices into two limiting shapes: an irregular *n*-sided polygon with an extended vertex or an irregular $n - 1$ sided polygon (see symbols in Fig. 3a and Supplementary Fig. S2). This shape transformation is analogous to the transformation between a sphere and a cone. Previous work on self-assembly of sticky cones has shown that a precise sequence of convex clusters form at magic numbers determined by the cone shape.[44,45] To quantify the transformation, we introduce a deformation parameter ξ as defined in Fig. S2a. This parameter provides a means of geometrically connecting the two limiting cases, the *n*-1 sided polygon ($\xi = 0$) and the pointy *n*-sided polygon ($\xi = 1$), which can exhibit very different phase behavior. Notice that the maximum amount of lateral vertex displacement towards and away from the polygon center is determined by the inward pinching ($\xi = 0$). Fig. 3a shows the faceting vs. pinching phase behavior of transformed polygons. At $\xi = 0.5$, the regular *n*-gons are shown and colored based on the crystal structures observed in Fig 2. If a pinched *n*-gon self-assembles structures that are crystallographically distinguishable from that of the regular (unpinched) *n*-gon, the polygonal symbol in the phase diagram is colored differently from that of the regular polygon at $\xi = 0.5$. We find that at low *n*, the pinch transformation can have a dramatic effect on assembly leading to degenerate (low pinching) and aperiodic (pinched heptagons) structures. In contrast, at higher *n* the assembly is not affected because the *n*-gon becomes concave for small inward pinching deformation and we only focused on convex shapes (See Model and Method Section), thus the amount of pinching is negligible at high *n*.

Pinched triangles self-assemble hierarchical rhombic tiling, where triangles coupled into rhombs pointing in the same direction (Fig. 3b). The pinch transformation of the square stabilizes two kite assemblies shown in Fig. 3c and d. A kite is a specific quadrilateral with two pairs of adjacent equal-length sides kites are a prototile of the famous Penrose quasicrystal tiling.[46] We find both a hierarchical and alternating kite crystal structure formed via self-assembly. The hierarchical kite tiling occurs at $\xi = 0.25$ and $n = 4$ (Fig. 3c). The rhombus tiling is similar to the (4^4) Archimedean tiling except for a shift between each row of rhombi due to the small protrusion of the pinched vertex (Fig. 3c). Hierarchical crystals of nanoparticles have been shown to have interesting mechanical[47] and electronic[48] properties. Further outward pinching leads to the formation of alternating complex structures whose centers lay on an oblique lattice (Fig. 3d).

The pinch transformation of the pentagon leads to two distinct crystal structures: the hierarchical rectangular tiling at $\xi = 0.0$ (Fig. 3e) and a pentagonal Cairo tiling at $\xi = 0.25$ (Fig. 3f). At lower ξ, a hierarchical rectangular crystal structure forms. Its unit cell consists of two pinched pentagons that collectively form a trapezoid the rectangular crystal structure is similar to the (4^4) Archimedean tiling except that the tiling is stretched along the apothem of the building block. The pentagonal Cairo tiling is the dual of the $(3^2.4.3.4)$ Archimedean tiling, and is also referred to as the $((5^3)^2.5^4.5^3.5^4)$ McMahon net.[49] Fe atoms in $Bi_2Fe_4O_9$ compounds are arranged on a pentagonal Cairo tiling.[50] Also, three- and four-arm DNA junction tiles have been shown to self-assemble the pentagonal Cairo tiling.[51]

The pinch transformation applied to the hexagon results in the assembly of three new crystal structures: a prismatic hierarchical tiling at $\xi = 0.0$ (Fig. 3g), a shifted prismatic hierarchical tiling at $\xi = 0.1$ (Fig. 3h) (closely related to the prismatic pentagonal tiling) and an alternating hexagonal tiling at $\xi = 1.0$. The prismatic pentagonal tiling is the dual of the $(3^3.4^2)$ Archimedean tiling. Three- and four-arm DNA junction tiles self-assemble the prismatic pentagonal tiling.[51] At high pinching ($\xi = 1.0$) (Fig. 3i), the pinched hexagon forms an alternating crystal structure similar to the (6^3) Archimedean tiling.

9

The pinch transformation applied to the heptagon produces the $(3^2.4.3.4)$ Archimedean tiling and the dodecagonal shield quasicrystal. At low ξ, the shield dodecagonal quasicrystal is stable (Fig. 3k). At high ξ, the $(3^2.4.3.4)$ Archimedean tiling is stable (Fig. 3k). A disordered region exists around the regular heptagon at intermediate ξ. It is interesting to note that the $(3^2.4.3.4)$ Archimedean tiling, also known as the σ-phase,[52] is a periodic approximant of a dodecagonal quasicrystal. Simple modifications of crystal growth rules have been shown to control the stability region of the $(3^2.4.3.4)$ Archimedean tiling and the dodecagonal triangle square tiling.[53] Patchy particles with seven patches symmetrically arranged on a disk has been shown to form a dodecagonal quasicrystal.[54] It is notable that for patchy heptagons, the quasicrystal is stable for an irregular arrangement of facets on the polygonal nanoplates. The pinch transformation provides a means of transforming the disordered heptagon assembly into the $(3^2.4.3.4)$ Archimedean tiling and a dodecagonal quasicrystal.

For large n, the pinch deformation is constrained to small changes by convexity and vertex constraints. Compressed octagons ($\xi =0.0$) stabilize the $(3^3.4^2)$ Archimedean tiling (Fig. 3l). These uniform structure has been observed in systems of droplets bouncing on a vibrating liquid.[54] Highly pinched octagons form only degenerate hexagonal assemblies (Fig. 3m). Nonagons and decagons at high $\xi >$ 0.75 form a triangular crystal (Fig. 3n). For the undecagon, dodecagon, and tridecagon, pinching has no effect on assembly because the applied pinch is too small given the constraints. Tilings comprised of nanoplates and polygonal pores ("empty tiles") as shown in Figs 3b-n have not yet been reported in experiments. Structures shown in Fig 3. j, k, l and m do not correspond to the densest packings and are the equilibrium states because NPT simulations show that at intermediate densities these porous structures are also observed, and upon further compression a transition towards the densest packings are achieved.

3.3. Elongation

The elongation transformation alters the shape of the n-gons by lengthening two opposite edges of regular polygons. Note that this transformation can be applied systematically only to polygons with an even number of facets. The elongation transformation is equivalent to the transformation between a sphere and a spherocylinder. The transformation is also closely related to the elongation along an axis of a sphere to form an ellipsoid. Patchy and hard spherocylinders[56,57] and ellipsoids[58,59] are the natural systems against which to compare the phase behavior of elongated or compressed polygons. The deformation parameter ζ quantifies the degree of elongation as defined in Fig. S2b. Except for squares, at $\zeta = 0$ two opposite edges of a regular n-gon are fully compressed until they vanish, reducing the number of edges and vertices to $n - 2$. As ζ increases, these opposite edges are elongated until regular polygons ($\zeta = 0.5$) are recovered, and for values of $\zeta > 0.5$ this shape transformation alters polygons into faceted rods. For $\zeta = 1.0$ the larger sides of the elongated polygons are twice the size of the regular n-gon at $\zeta = 0.5$. In Fig. 4a, the effect of elongation on n-gons ($n = 4, 6, 8, 10$ and 12) is displayed in a faceting vs. elongation "phase" diagram, where colored symbols showed the modified shape of the elongated particles (Fig. 4a).

Slightly elongated squares self-assemble degenerate rectangular tilings closely related to the (4^4) Archimedean tiling. For $\zeta > 0.25$ self-assembly into structures lacking global order is observed. Elongated hexagons ($n = 6$) self-assemble into three distinct crystal structures: a random tiling for $\zeta \sim$ 0.0, a rhombic tiling, and an elongated (6^3) Archimedean tiling (Fig. 4c). At $\zeta = 0.0$ the polygon is a rhombus shape ($n = 4$ with angular openings of 60 degrees at the tips) and forms a random tiling in accordance with previous theoretical and experimental studies.[60]

For the case of octagons ($n = 8$), low and high elongation leads to the formation of triangular and stretched (4.8^2) Archimedean tilings, respectively. At zero elongation ($\zeta = 0.0$), a triangular tiling is formed (Fig. 4e), whereas at high elongation ($\zeta = 1.0$), the elongated octagons form a stretched (4.8^2) Archimedean tiling (Fig. 4f).

11

The elongated decagon (n = 10) forms an alternating and a stretched rhombic crystal structure (Fig. 4g and h). At $\zeta = 0$, the alternating crystal consists of alternating rows of oppositely oriented building blocks. The unit cell of this crystal consists of two decagons with different orientation and tiles space in a rectangular lattice (Fig. 4g). To our knowledge, the alternating elongated decagon crystal structure has not yet been observed experimentally. At high elongation ($\zeta = 0.8$), irregular decagons assemble a stretched rhombic crystal (Fig. 4h).

The elongated dodecagon (n = 12) forms a triangular tiling and a stretched Archimedean tiling (Fig. 4i and j). At lower elongation ($\zeta = 0$), the dodecagon forms a triangular lattice that is rotationally degenerate (Fig. 4i). At $\zeta = 1$, the elongated dodecagon forms a stretched (3.12^2) Archimedean tiling Fig. 4j). In a similar way to the elongated hexagon, octagon, and decagon, the elongated dodecagon effectively stretches the crystal structure formed by the regular dodecagon.

The elongation transformation is not symmetric low and high elongation n-gons do not self-assemble the same crystal structure. In contrast, it is interesting to note that the phase diagram of hard ellipsoids is symmetric,[55] which implies that faceting can have an important effect on the assembly of nanorods at low aspect ratio. For nanoplates, the elongation transformation has been previously studied for lanthanide fluoride (LaF$_3$) nanoplates both experimentally and with simulations.[25] The experimental results in that work are similar to the tilings shown in Figs 4c-e. Simulation results revealed that for systems with symmetric interactions, parallel arrangements were stable regardless of the degree of elongation entropic interactions favored such arrangements, and the introduction of symmetric forces (comparable to thermal energies) were not expected to disrupt this trend.[25] Also, simulations revealed that high elongation leads to the formation of tetragonal lattices because these arrangements maximize the amount of contact between neighboring particles, thereby minimizing the total free energy.[25] The porous tilings shown in Figs 4e-i have not yet been reported in experiments.

3.4. Truncation

The truncation transformation of faceted nanoplates alters the geometry of the n-gons by truncating each vertex symmetrically into an edge. The symmetric truncation transformation has no analogue in continuous geometries (disks and ellipses), and is characteristic of faceted nanoparticles. Symmetric truncation transforms a regular polygon with n vertices into another polygon with twice ($2n$) the number of vertices (see symbols in Fig. 5a). We connect these two limiting cases by representing the n-sided regular polygons with $\gamma = 0.0$ and the $2n$-sided polygons with $\gamma = 1.0$ as defined in Fig. S2c. We introduce a deformation parameter γ to quantify this transformation. We show the phase behavior of each nanoplate in a geometric phase diagram plotting faceting vs. truncation (Fig. 5a). Regular n-gons are obtained at $\gamma = 0.0$ and $\gamma = 1.0$ and symbols colored according to their corresponding crystal structures are shown as in Fig 2. The truncated n-gons used to obtain the assemblies are shown in the phase diagram panel (Fig. 5a). Truncation has an effect on self-assembly for small n, but at larger n the particles exhibit phase behavior similar to that of a disk at high density.

Truncation continuously transforms the triangle ($n = 3$) into a hexagon ($n = 6$). Triangles and hexagons form (3^6) and (6^3) and Archimedean tilings, respectively. In 3D, truncation of tetrahedra leads to multiple transitions among quasicrystal, diamond, beta-tin, high pressure lithium and bcc crystal structures.[61] However, in 2D, we find that the effect of truncation is less profound. The truncated triangle modifies the (3^6) Archimedean tiling by adding hexagonal pores with areas proportional to the degree of truncation while still preserving a nearest-neighbor shell of three particles per polygon (Fig. 5b). These porous tilings have not yet been reported in experiments. Halfway between triangles and hexagons ($\gamma \sim 0.65$), the irregular polygon, now with six edges, changes coordination number from three to six and can point randomly in six different directions, forming a rotationally degenerate hexagonal lattice. The change in coordination number indicates the onset of a transition towards the (6^3) Archimedian tiling from a honeycomb structure. Indeed, at $\gamma = 1.0$ the polygon becomes a regular hexagon and the (6^3) Archimedian tiling is formed. The transformation between the (3^6) Archimedean tiling to the (6^3) Archimedean tiling shows that shape transformation can have subtle, gradual effects on the assembled structures.

13

The truncated square ($n = 4$) and octagon ($n = 8$) form crystals that are closely related. The truncated square at intermediate truncation $\gamma = 0.25$ forms a Mediterranean tiling (Fig. 5c). The Mediterranean tiling is similar to the (4.8^2) Archimedean tiling but the square tile is either smaller or truncated. These porous structures have been realized in osmotically concentrated monolayers of microplatelets. [62] a slightly truncated heptagon forms dodecagonal quasicrystals.

The truncated heptagon stabilizes a dodecagonal quasicrystal similar to the one observed for this polygon under the pinch transformation (Fig. 5d). This complex aperiodic structure forms for low and intermediate truncation values ($0.25 \leq \gamma < 0.75$). Such tilings have not yet been reported in experimental self-assembly of nanoplates. At higher truncation $\gamma = 0.75$, the truncated heptagon acts like a tetradecagon and forms porous center lattices (Fig. 2m). The proximity in shape space of these two structures motivates the possibility of a switchable structure.

The truncated octagon forms an irregular star polygon tiling. This irregular star polygon tiling is closely related to the $(8.4^*_{\pi/4}.8.4^*_{\pi/4})$ regular star polygon tiling formed by symmetric truncation.[63] Oblique closed packed assemblies of PbS nanostars have been achieved by vertical deposition.[64] However, the porous tilings illustrated in Figs 5c and e have not yet been reported in experimental (2D) self-assembly of nanoplates. The truncated octagon provides a simple means of obtaining a patterned array of star-shaped pores (Fig. 5e). Slight truncation of regular n-gons with a large number of vertices alters the pore structure, but not the coordination of the crystal structure. Highly truncated octagons are similar to hexadecagons in shape and thus form sheared $(3^2.4.3.4)$ Archimedean tilings (Fig.S8).

3.5. Discussion

The shape optimization of faceted nanoplates for assembly begins with understanding the effect of different shape transformations on the assembly of polygons representing nanoplates. Specific shape

transformations provide the material designer with new design axes to synthesize new functional materials (See Fig.7 and Fig. S3-S12). For example, we showed that truncation and elongation allow the synthesis of porous tilings such as porous alternating tilings and porous mediterrenean tilings (Fig. 4g, 5e and 7a,c), pinching allows for the stabilization of the pentagonal Cairo tiling (Fig. 7b) or the prismatic pentagonal tiling (Fig. 3e, f), and poor assemblers in the regular n-gon family, such as the nonagon, heptagon, and pentagon, can be self-assembled into crystals by judicious use of one of the shape transformations discussed (Figs. 6 and 7b,d).

Our results can be summarized into three classes of tilings: space-filling, porous, and "complex" (Fig. 6a,b and c). Colored arrows indicate which of the four transformations, when applied on a given shape, results in one of the three classes mentioned above. Some structures can be simultaneously in two of these categories. Also, degenerate crystal structures appear after applying small transformations. Space-filling tilings form from regular triangles, squares and hexagons (Fig. 6a). This is expected since these polygons constitute the tiles that form regular Archimedean tilings. Also, moderate pinching of these regular polygons and elongation exclusively applied to hexagons leads to space-filling assemblies. Porous tilings (Fig. 6b) are formed by regular octagons, decagons, undecagons, dodecagons and tridecagons. Truncated triangles, squares, hexagons, heptagons, octagons and undecagons also form porous tilings. The benefit of using irregular faceted polygonal nanoplates is that the pore size can be dynamically tuned in experiments via truncation using photodecomposition.[65] Complex tilings with multiple nanoplates in a unit cell (Fig. 6c) is observed for irregular triangles, square pentagons, hexagons, heptagons and decagons. The majority of the complex tilings occur due to the pinch transformation and at low n (Fig. 6c). Other interesting complex tilings we observe include the pentagonal Cairo tiling (Fig. 3e). The location of these interesting structures in the geometric phase diagram (pinched, small n polygonal nanoplates) should motivate experimental studies on monodisperse irregular nanoplates. The rotationally degenerate complex tilings are found in pinched nonagons, decagons and elongated dodecagons. A degenerate structure from irregular dodecagons is expected because elongated "pear-like" colloidal dimers also form disordered rotator

crystals.[65] On the other hand, the degenerate crystal structure of asymmetric pinched nonagons and decagons is analogous to the assembly of hard asymmetric dimers.[66]

Looking beyond the present study, highly symmetric faceted nanoparticles such as the Johnson and Archimedean polyhedra have been predicted to form crystals ranging from quasicrystals to diamond to Frank-Kasper crystals with large unit cells.[7] The shape transformations studied here can increase or decrease the symmetry of effectively two-dimensional versions of faceted nanoparticles such as those. The elongation and pinch transformations decrease the symmetry of the building block but these building blocks stabilize complex and porous tilings (Figs. 3, 4 and 6). In contrast, the truncation transformation increases the symmetry of the building block and stabilizes porous and lattice tilings (Figs. 5 and 6). These two results highlight, again, that the symmetry of the building block may not be a sufficient indicator to predict the self-assembly prospects of a material.[7] Experimental work to synthesize irregular nanoplates could lead to significant progress in understanding the effect of symmetry and shape on self-assembly.

From the perspective of material optimization, the improved assembly properties of the regular heptagon highlight the power of shape transformations. The frustrated (non)-assembly of the regular heptagon has two local motifs at low densities: the $(3^2.4.3.4)$ Archimedean tiling and the shield-triangle tiling. Both motifs are observed in the shield dodecagonal quasicrystal. The pinch transformation allows for the self-assembly of the $(3^2.4.3.4)$ Archimedean tiling and the dodecagonal quasicrystal structures by relaxing geometric constraints (overlapping) between heptagons when attempting to locally form triangular arrangements. Similarly, truncation applied to heptagons relaxes local geometric constraints, allowing for the formation of dodecagonal quasicrystals. These shape transformations provide a means of toggling among different structures in the case of active (*in-situ*) shape change.[67-72] The judicious use of geometric transformations could lead to the self-assembly of new exotic structures.

16

4. Conclusions

Building an experimental toolbox for self-assembly as a systematic design framework could transform the field of self-assembly from a basic scientific discipline to an engineering discipline. We showed that continuous shape transformation in the presence of short-ranged attractive forces stabilizes space-filling, porous and complex tilings at intermediate densities. The proposed design rules constitute a first step towards the understanding of shape optimization and highlight a deeper study of its effect on self-assembly. The development of heuristic rules for shape optimization would allow experimentalists to tune the shapes of anisotropic building blocks to select and improve the crystal properties of target assemblies. Furthermore, an understanding of the mechanisms to improve the assembly propensity of certain structures could allow for *a priori* screening of materials. Previous work shows that the fabrication of high performance nanocrystal-based devices[73-77] with tunable interparticle spacing and electronic coupling,[73] which can lead to enhance thermopower.[76] Porous ZnO nanoplate structures are strong candidates for low-cost dye-sensitsed solar cells.[78] These novel properties have applications to such diverse as solar energy, military and cosmetics, among others. We look forward for further experimental developments to validate the material design principles provided in this contribution.

17

Notes and References

Footnotes

‡ J.A. Millan and D. Ortiz contributed equally to this work.

†Electronic Supplementary Information (ESI) available: See DOI: 10.1039/b000000x/

1. R. Narayanan and M.A. El-Sayed. *J. Phys. Chem. B,* 2005, **109**, 12663–76.

2. B. J. Wiley, S. H. Im, Z.-Y. Li, J. McLellan, A. Siekkinen and Y. Xia, *J. Phys. Chem. B,* 2006, **110**, 15666–75.

3. T. Jensen, L. Kelly, A. Lazarides and G.C. Schatz, *J.Clust. Sci.* 1999, **10**, 295-317.

4. C. Soukoulis and M. Wegener, *Nat. Photonics,* 2011**, 5**, 523-30.

5. Lv Shanshan, D.M. Dudek, Y. Cao, M. M. Balamurali, J.Gosline J. and H. Li, *Nature,* 2010**, 465**, 69-73.

6. P. F. Damasceno, M. Engel and S. C. Glotzer, *Science*, 2012, **337**, 453–7.

7. Y. C. Cao, *J. Am. Chem. Soc.* 2004, **126**, 7456–7.

8. Y. Zhang, X. Sun and R. Si, *J. Am. Chem. Soc.*, 2005, **127 (10)**, 3260–61

9. Y. Sun and Y. Xia, *Adv. Mater.* **2003**, *15*, 695–99.

10. L. Kavan, J.-H. Yum and M. Grätzel, *Nano Lett.* 2011, **11**, 5501–6.

11. L. Lu, A. Kobayashi, K. Tawa and Y. Ozaki, *Chem. Mater.*, 2006, **18**, 4894–4901.

12. S. Pal, Y. K. Tak and J. M. Song, *Appl. Environ. Microbiol.*, 2007, **73**, 1712–20.

13. C. Chao, Z. Ren, , S. Yin, S. Gong, X. Yang G. Xu, , X. Li, G. Shen and G. Han *Cryst. Eng. Comm.,* 2013, **15**, 8036-8040.

14. Y. Kim, H. Han, Y. Kim, W. Lee, M. Alexe, S. Baik and J. K. Kim, *Nano Lett.*, 2010, **10**, 2141–6.

15. Z. Deng, M. Mansuripur and A. J. Muscat, *J. Mater. Chem.*, 2009, **19**, 6201.

16. Z. Quan, J. Fang, *Nano Today*, 2010, **5**, 390–411.

17. Y. Kang, M. Li, Y. Cai, M. Cargnello, R. E. Diaz, T. R. Gordon,N.L. Wieder, R. Adzic, R.J. Gorte, E. A. Stach and C. B. Murray, *ACS Nano*, 2013, **135(7)**,22741-2747.

18. M. P. c

19. A. R. Tao, S. Habas and P. Yang, *Small*, 2008, **4**, 310–25.

20. M. M. Maye, M. T. Kumara, D. Nykypanchuk, W. B. Sherman and O. Gang, *Nature Lett. ,*2010, **5**, 116–20.

21. T. D. Nguyen, E. Jankowski and S. C. Glotzer, *ACS Nano* , 2011, **5**, 8892–903.

22. T. D. Nguyen and S. C. Glotzer, *ACS Nano*, 2010, **4**, 2585–94.

23. S. C. Glotzer and M. J. Solomon, *Nat. Mater.*, 2007, **6,** 557–62.

24. G. van Anders, N. K. Ahmed, D. Klotsa, , M. Engel and S. C. Glotzer *arXiv:1309.1187* 2013.

25. X. Ye, J. Chen, M. Engel, J. A. Millan, W. Li, L. Qi, G. Xing, J. E. Collins, C. R. Kagan and J. Li, *et al*. *Nat. Chem.*, 2013, **5**, 466–73.

26. S. Porel, S. Singh and T. P. Radhakrishnan, *Chem. Commun. (Camb).* 2005, **18**, 2387–9.

27. C. Kan, C. Wang, H. Li, J. Qi, J. Zhu, Z. Li and D. Shi, *Small* 2010, **6**, 1768–75.

28. M. Tsuji, X. Tang, M. Matsunaga, Y. Maeda and M. Watanabe, *Cryst. Growth Des*. 2010, **10**, 5238–43.

29. M. Pradhan, S. Sarkar, A. K. Sinha, M. Basu and T. Pal, *Cryst.Eng. Comm*, 2011, **13**, 2878-2889.

30. A. A. Umar, M. Oyama, M. M. Salleh and B. Y. Majlis, *Cryst. Growth Des.*, 2009, **9,** 2835–2840.

31. H.-C. Chu, C.-H. Kuo and M. H. Huang, *Inor. Chem.*, 2006, **45**, 808–13.

32. B. Tang, S. Xu, J. An, B. Zhao and W. Xu, *J. Phys. Chem. C* 2009, **113**, 7025–7030.

33. Y. Min, M. Akbulut, K. Kristiansen, Y. Golan and J. Israelachvili, *Nat. Mat.* 2008, **7**, 527-538.

34. Z. Tang, Z. Zhang, Y. Wang, S.C. Glotzer and N. A. Kotov, *Science*, 2006, **304**, 274-78.

35. L. Li and A. P. Alivisatos, *Phys. Rev. Lett.* 2003, **90,** 097402.

36. T. Nann, Schneider, *J. Chem. Phys. Lett.* 2004, **384**, 150–152.

37. S. A. Maier, P. G. Kik and H. A. Atwater, *Phys. Rev. Lett. B,* 2003, **67,** 205402.

38. E. Rechberger, A. Hohenau, A. Leitner, J.R. Kren, B. Lamprecht, F.R. Aussemegg, *Opt. Comm.*, 2003, **220,** 131-41.

39. Y. L Duparcmeur, A. Gervois and J. P. Troadec, *Phys. I* 1995, **5**, 1539-1550.

40. J. A. Millan, D Ortiz and S. C. Glotzer *ACS Nano* 2014, **8(3)** 2918-2928.

41. D.R. Nelson, *Phys. Rev. B*, 1983**, 28 ,** 5515-35 .

42. L. Merz, M. Parschau, J. S. Siegel and K.-H. Ernst, *Chem. Int. J. Chem.*, 2009, **63**, 214–216.

43. S. P. Gorkhali, J. Qi and G. P. Crawford, *J. Opt. Soc. Am. B* 2006, **23**, 149.

44. T. Chen, Z. Zhang and S. C. Glotzer, *Langmuir***,** 2007, **23**, 6598–605.

45. T. Chen, Z. Zhang and S.C. Glotzer, *PNAS*, 2007, ***104(3),*** 717-22.

46. H. C. Jeong and P. J. Steinhardt, *Phys. Rev. B*, 1997, **55**, 3520–3532.

47. K. Miszta, J. Graaf, G. de Bertoni, D. Dorfs, R. Brescia, , S. Marras, L. Ceseracciu, R. Cingolani, R. Roij, M. Dijkstra and M. Liberato, *Nat. Mater.*, 2011, **10**, 872–6.

48. Y. Tao, Y. Shen, L. Yang, B. Han, F. Huang, S. Li, Z. Chu and A. Xie, *Nanoscale*, 2012, **4**, 3729–33

49. M. O'Keeffe and B. G. Hyde, *Philos. Trans. R. Soc. A Math. Phys. Eng. Sci.*, 1980, **295**, 553–618.

50. E. Ressouche, V. Simonet, B. Canals, M. Gospodinov and V. Skumryev, *Phys. Rev. Lett.*, 2009, **103**, 267204.

51. F. Zhang, Y. Liu and H. Yan, *J. Am. Chem. Soc.* 2013, **135**, 7458–61.

52. P. Stampfli, *Helv. Phys. Acta*, 1986**, 59,** 1260-1263.

53. K. Kuo, Y. Feng and H. Chen, *Phys. Rev. Lett.*, 1988, **61**, 1740–1743.

54. A. Eddi, A. Decelle, E. Fort nad Y Couder, *Europhys. Lett.*,2009, **87**, p1-56002-p6

55. M. van der Linden, J. Doye and A. Louis, *J. Chem. Phys.*, 2012, **136**, 054904.

56. J. Veerman and D. Frenkel, *Phys. Rev. A,* 1990, **41***,* 3237-3244.

57. R. Vácha and D. Frenkel, *Langmuir*, 2014, **30 (5)**, 1304–1310

58. D. Frenkel, B. M. Mulder and J. P. McTague , *Phys. Rev.*, 1984**, 52**, 287-290.

59. Y. Liu, W. Li, T. Perez, J. D. Gunton and G. Brett, *Langmuir*, 2012, **28**, 3–9.

60. M. O. Blunt, J. C. Russell, M.C. Gimenez-Lopez, J.P. Garrahan, X. Lin, M. Schroeder, N.R. Champness and P.H. Beton, *Science*, 2008, **322**, 1077-81.

61. P. Damasceno, M. Engel and S.C. Glotzer, *ACS Nano,* 2012, **6**, 609-614.

62. K. Zhao, R. Bruinsma and T.G. Mason, *PNAS,* 2011, **108**, 2684-2687.

63. B. Grünbaum and G. Shephard, *Math. Magazine*, 1977, **50 (5)**, 227-47.

64. T. Huang, Q. Zhao, J. Xiao and Q. Limin, *ACS Nano*, 2010, **4 (8)**, 4707-4716.

65. X.F. Wu, H.Y Song, J.M. Yoon, Y.T Yu and Y.F. Chen, *Langmuir*, 2009, **25(11)**, 6438–6447.

66. S.H. Lee , I.D. Y. Song, Hosein, C. M. Lidell, *J. Mater. Chem.*, 2009, **19**, 350-355.

67. T.D. Nguyen and S.C. Glotzer, *Soft Matter*, 2010, **4**, 2585-2594.

68. O. Gang and Y. Zhang, *ACS Nano,* 2011, **5 (11)**, 8459–8465.

69. Y.G. Zhang, F. Lu, , D. van der Lelie and O. Gang, *Phys. Rev. Lett.,* 2011, **107**, 135701.

70. K.F. Bian, J. J. Choi, A. Kaushil, P. Clancy, D.M. Smilgies and T. Hanrath, *ACS Nano*, 2011, **5**, 2815-2823.

71. Y. Yang, S. Matsubara, L. Xiong, T. Hayakawa and M. Nogami, *J. Phys. Chem. C,* 2007, **111**, 9095–9104.

72. T. K. Sau and C. J. Murphy, *Langmuir*, 2004, **20**, 6414–20.

73. D. V. Talapin and C.B. Murray, *Science*, 2005, **310**, 86-89

74. S. Sun.; C.B. Murray; D. Weller; L. Folks and A. Moser, *Science*, 2000, **287**, 1989-1992.

75. A. Dong; X. Ye; J. Chen and C.B. Murray, *Nano Lett.*, 2011, **11 (4)**, 1804-1809

76. R. Y. Wang; J. P. Feser; J. Lee; D. V. Talapin; R. Segalman; and A. Majumdar, *Nano Lett.*, 2008, **8**, 2283-2288.

77. J. M. Luther; M. Law; Q. Song; C. L. Perkins; M. C. Beard and A. J. Nozic, *ACS Nano*, 2008, **2 (2)**, 271-280

78. Y. Qiu; W. Chen and S. Yang, *J. Mater. Chem.*, 2010, **20**, 1001-1006.
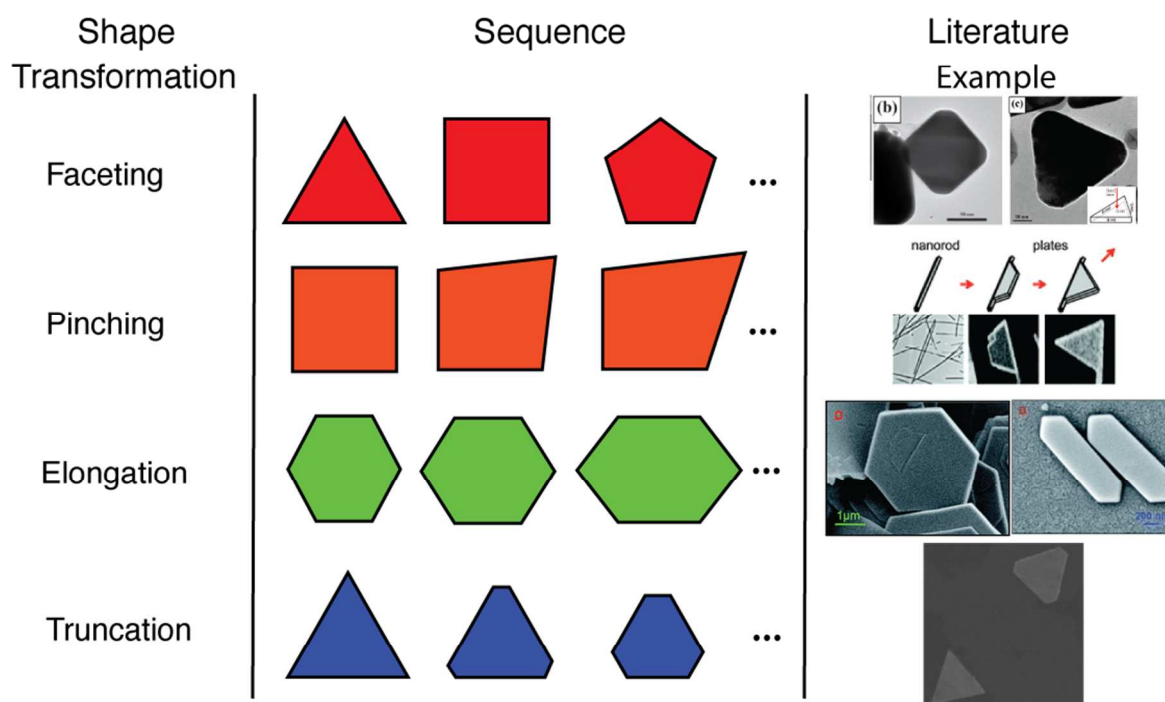
Fig.1 Shape transformations for nanoplates. The first column corresponds to the classification of experimentally observed shape transformations corresponding to faceting, pinching, elongation, and truncation. The second column depicts the effect of each transformation on particle shape. Experimental examples of each transformation are shown in the third column. The faceting shape transformation is shown for silver nanoplates.[72] The pinch transformation is shown for the growth of a silver triangular nanoplate on a nanorod.[28] The elongation transformation is shown for uranimum oxide hydroxide hexagonal nanoplates.[29] The truncation transformation is shown for hexagonal and triangular nanoplates.[30]
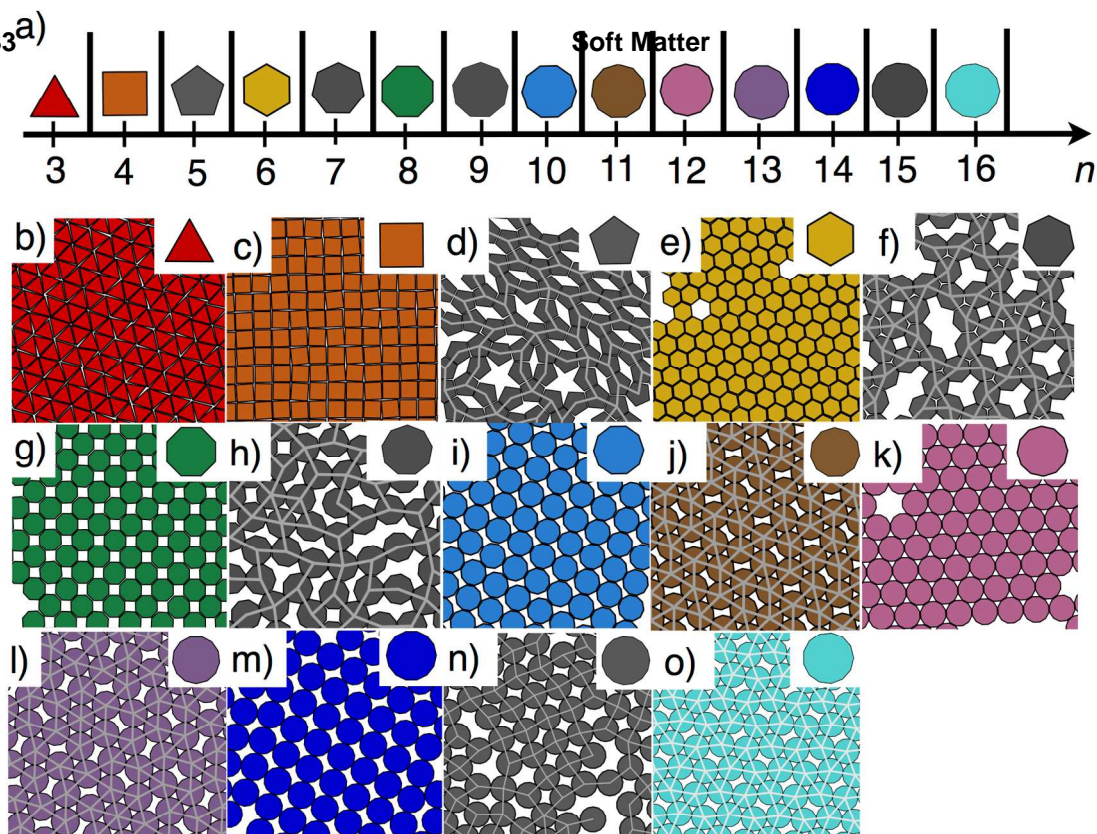
Fig. 2. Self-assembly of *n*-gons. (a) The faceting transformation is summarized by a geometric axis showing the regular polygons. Grey n-gons imply a frustrated assembly, while a colored regular *n*-gon indicates that shape assembles into a crystal. (b-l) Each snapshot shows a portion, cut from a larger sample containing as many as 1000 nanoplates, of a representative assembly of the nanoplates. The assemblies for the regular *n*-gon family are (b) the (3^6) Archimedean tiling for the regular triangle ($n = 3$), (c) the (4^4) Archimedean tiling for the regular square ($n = 4$), (d) a frustrated assembly for the regular pentagon ($n = 5$), (e) the (6^3) Archimedean tiling for the regular hexagon ($n = 6$), (f) a frustrated assembly for the regular heptagon ($n = 7$), (g) the (4.8^2) Archimedean tiling for the regular octagon ($n = 8$), (h) a frustrated assembly for the regular nonagon ($n = 9$), (i) a sheared rhombic tiling for the regular decagon ($n = 10$), (j) a sheared $(3^2.3.4.3)$ Archimedean tiling for the regular undecagon ($n = 11$), (k) the (3.12^3) Archimedean tiling for the regular dodecagon ($n = 12$), (l) a sheared $(3^2.3.4.3)$ Archimedean tiling for the regular tridecagon ($n = 13$), (m) a center rectangular tiling formed for the regular tetradecagon ($n = 14$), (n) a disordered tiling for the regular pendecagon ($n = 15$) and (o) shear $3^2.3.4.3$) Archimedean tiling for the regular hexadecagon ($n=16$).
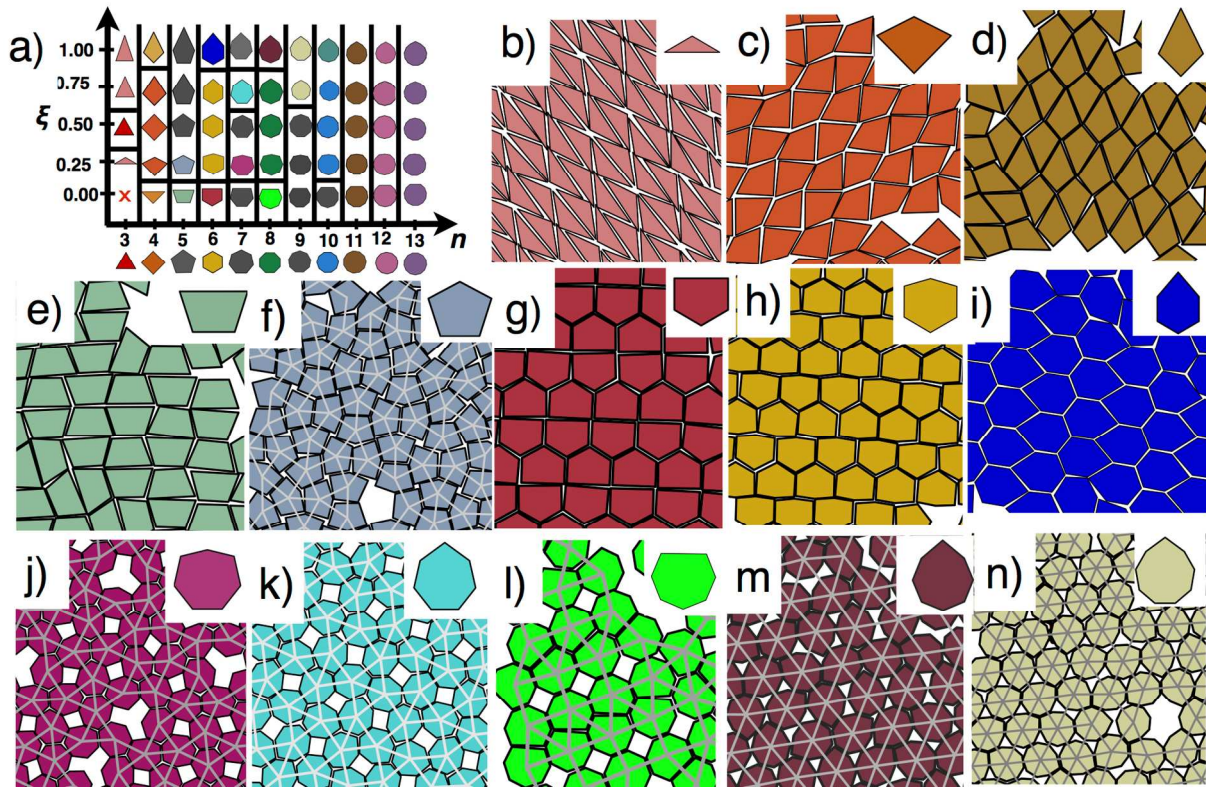
24

Figure 3. Effect of pinch transformation on the self-assembly of polygons. (a) Faceting vs. pinching phase diagram. Grey n-gons imply a frustrated assembly and heavy bars represent phase boundaries. The regular *n*-gons at ξ = 0.5 are shown with the symbols and crystal structures observed in Fig 2. The building blocks for each geometric phase point are shown in the geometric phase diagram. Representative snapshots of crystal structures (b-n) were self-assembled from pinched polygons that deviate from those formed from regular *n*-gons (ξ = 0.5). The assemblies for the pinched *n*-gon family are: (b) rhombic tiling assembly for compressed triangles ξ = 0.25 and *n* = 3, (c) a shortened kite assembly for ξ = 0.25 and *n* = 4, (d) a lengthened kite assembly for ξ = 0.75 and *n* = 4, (e) a trapezoidal assembly for ξ = 0.0 and *n* = 5, (f) a pentagonal Cairo tiling for ξ = 0.25 and *n* = 5, (g) prismatic tiling form compressed hexagons ξ = 0.00 and *n* = 6, (h) a shifted prismatic tiling for ξ = 0.25 and *n* = 6, (i) an alternating triangular tiling for ξ = 1.0 and n = 6, (j) a dodecagonal quasicrystal for ξ = 0.25 and *n* = 7, (k) a (3^2.4.3.4) Archimedean tiling for ξ = 0.75 and *n* = 7, (l) a (3^3.4^2) Archimedean tiling for ξ = 0.0 and *n* = 8, (m) a triangular tiling for ξ = 0.75 and *n* = 8, (n) a triangular tiling for ξ = 0.75 and *n* = 9.
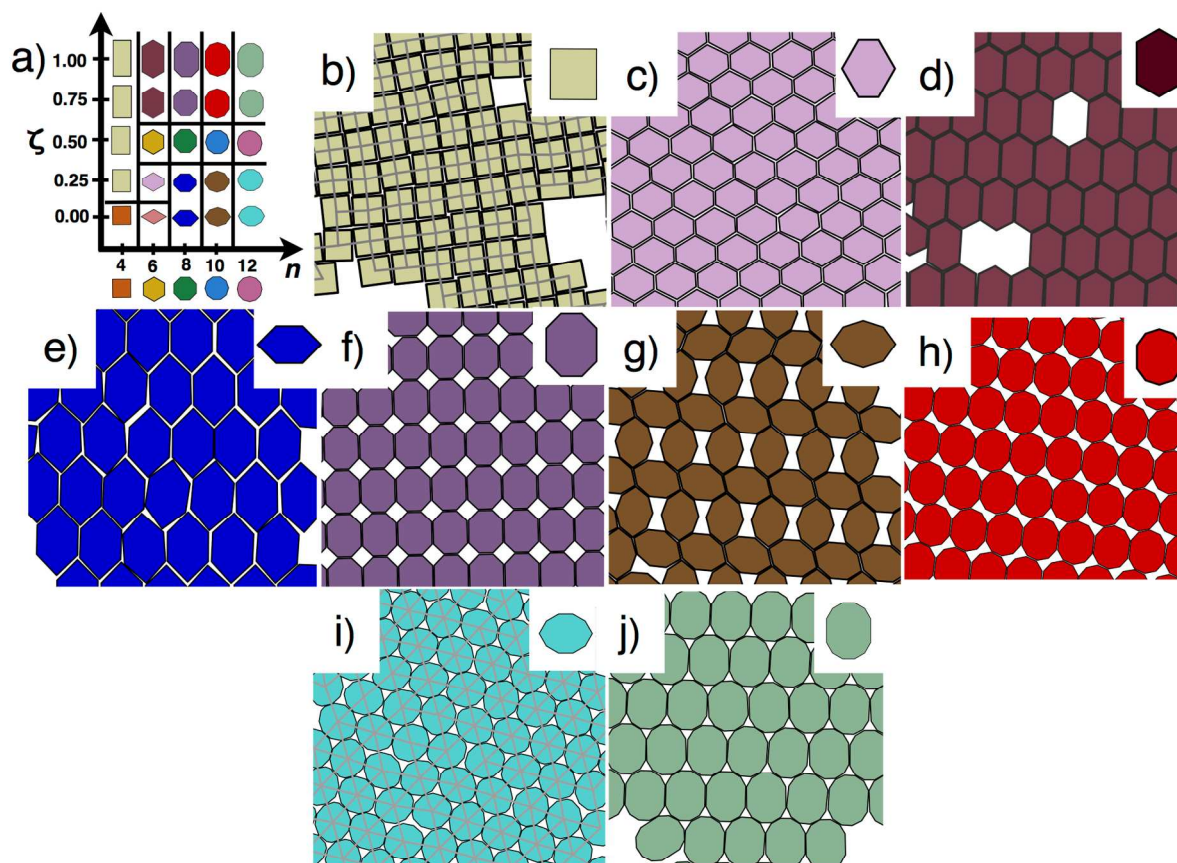
25

Figure 4. Effect of elongation on the self-assembly of polygons. (a) Faceting vs elongation phase diagram. The building blocks for each geometric state point are shown in the geometric phase diagram and heavy bars represent phase boundaries. Representative snapshots (b-j) of crystal structures were self-assembled from elongated polygons that deviate from those formed from regular n-gons (ζ = 0.5) are: (b) degenerate rectangular tiling for slightly elongated square (ζ = 0.1), (c) a space-filling structure for compressed hexagons (ζ = 0.25) hexagons (n = 6), (d) a space-filling structure for elongated (ζ = 0.8) hexagons (n = 6), (e) a space-filling tiling formed from fully compressed (ζ = 0.0) octagons (n = 8), (f) a stretched (4.8^2) Archimedean tiling for elongated (ζ = 0.8) octagons (n = 8), (g) a complex porous structure for fully compressed (ζ = 0.75) decagons (n = 10), (h) an oblique porous tiling for elongated (ζ = 0.8) decagons (n = 10), (i) a degenerate triangle lattice for compressed (ζ = 0.0, (j) an elongated (3.12^2) Archimedian tiling for elongated (ζ = 1.0) dodecagons (n = 12).
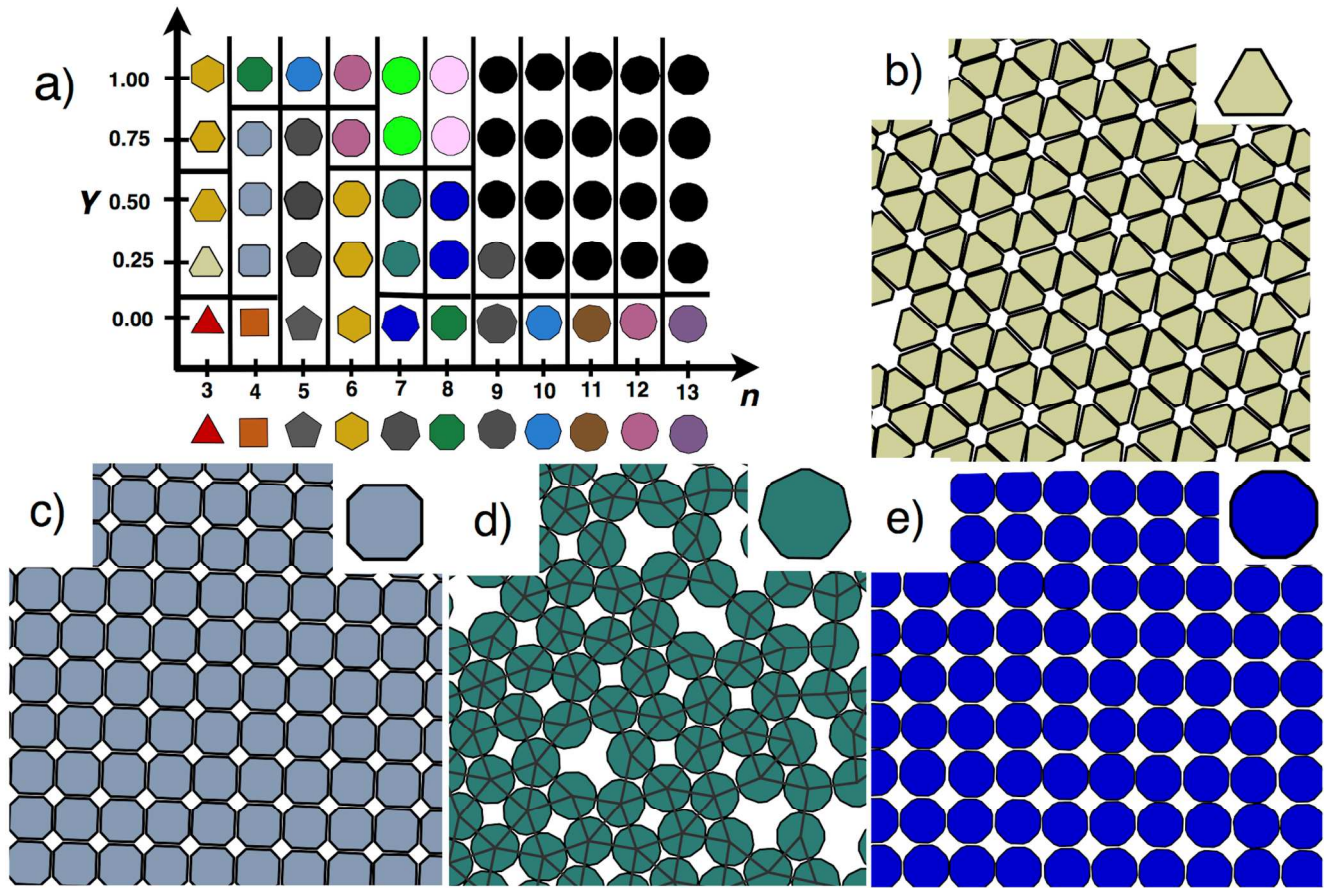
Figure 5. Effect of truncation on the assembly of polygons. (a) A geometric diagram for the faceting and truncation anisotropy dimensions shows the crystal phases observed. Dark Grey n-gons imply a frustrated assembly and heavy bars represent phase boundaries. The building blocks for each geometric state point are shown on the phase diagram. Representative snapshots of crystal structures (b-e) observed for truncated polygons that deviate from those structures observed for regular n-gons ($\gamma = 0$). (b) A porous (3^6) Archimedean tiling for slightly truncated ($\gamma = 0.25$) triangles ($n = 3$), (c) Mediterranean tiling for truncated ($\gamma = 0.5$) squares ($n = 4$), (d) dodecagonal quasicrystal at $\gamma = 0.38$ and $n = 7$, and (e) a regular star polygon tiling for truncated ($\gamma = 0.5$) octagons ($n = 8$).
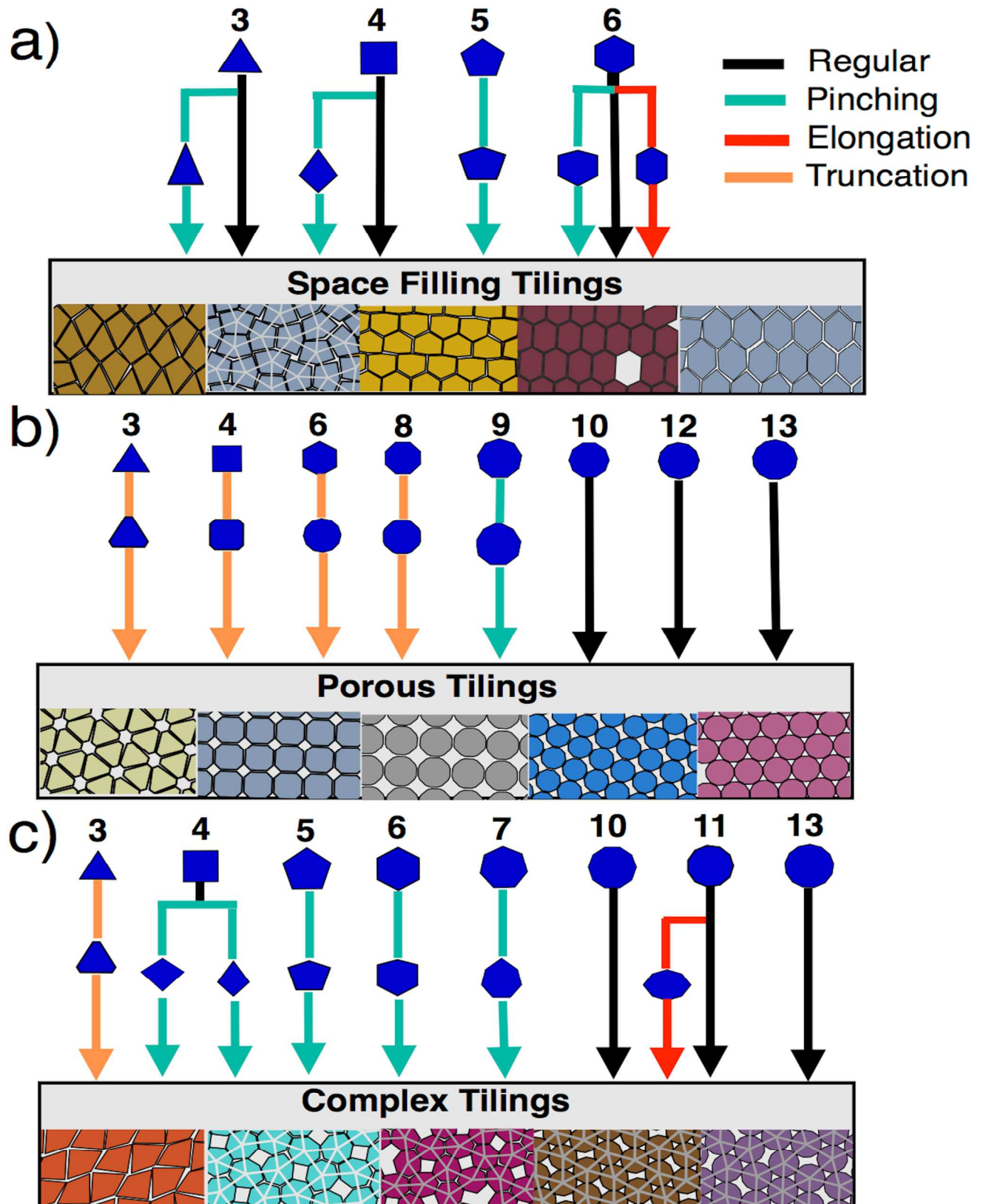
Figure 6. A classification of the different tilings observed as a function of shape transformation. (a) A summary of all the transformed polygons (nanoplates) that formed space-filling tilings. Judiciously pinched and non-pinched triangles, squares and hexagons assemble into space-filling tilings. Elongated hexagons formed structures that completely tile the two-dimensional plane. (b) Degenerate and regular porous structures form from truncated triangles, squares, hexagons, heptagons, octagons, nonagons, decagons, undecagons, dodecagons and tridecagons. Regular octagons, decagons, undecagons, dodecagons and tridecagons also form long-range ordered porous structures. (c) Complex structures can be assembled from pinched squares, pentagons, hexagons, heptagons, regular decagons, (elongated) undecagons and tridecagons. Colored-coded arrow indicate which of the four trnasfomrations , when applied on a given shape, results in one of three classes of tilings discussed.
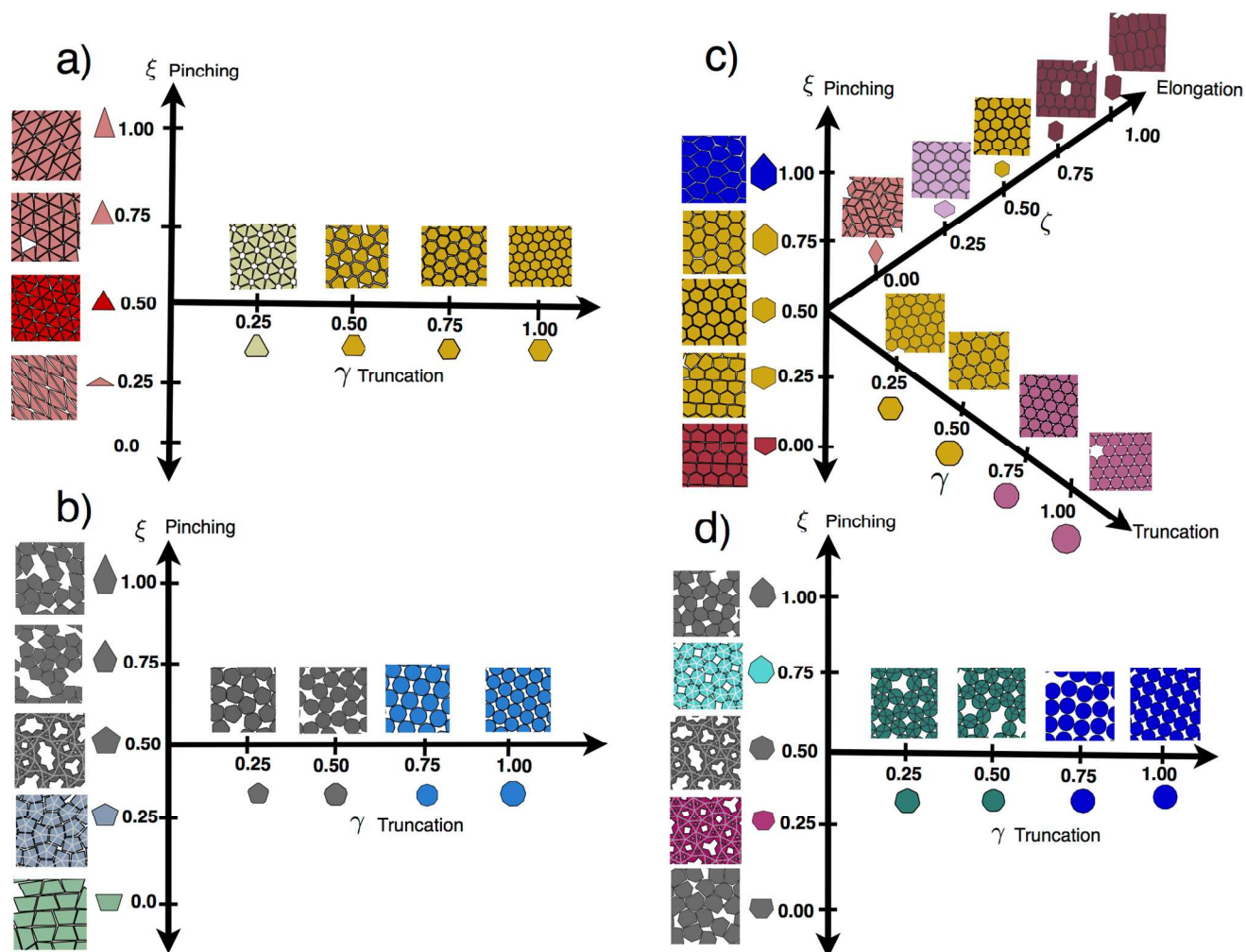
Figure 7. Phase behavior of triangles, squares, pentagons and heptagons along the pinching (ξ), elongation (ζ) and truncation (γ) deformations. (a) Pinching of triangles leads to the formation (3^3) Archimedean tiling ($\xi = 0.25$) and a rhombic tiling ($\xi = 0.25$ and $\xi = 0.75$ and 1.0). Truncation of triangles leads to the stabilization of a porous triangular tiling ($\gamma = 0.25$), degenerate ($\gamma \geq 0.25$) and non-degenerate ($\gamma = 0.75$ and 1.00) hexagonal (6^6) Archimedean tilings. (b) Pinched pentagons form a trapezoidal tiling ($\xi = 0.00$), a Cairo tiling ($\xi = 0.25$), frustrated ($\xi = 0.50$) and disorder assemblies ($\xi = 0.75$ and 1.0). Slight truncation of pentagons leads to disorder phases. For higher truncation values ($\gamma \geq 0.75$) oblique structures reminiscent of those formed from regular decagons (See Fig. 2i). (c)

30

Pinched hexagons form a prismatic structure ($\xi = 0.00$ and $\xi = 0.25$), a non-degenerate ($\xi = 0.50$) and a degenerate ($\xi = 0.75$) hexagonal (6^6) Archimedean tiling, and an alternating triangular tiling ($\xi = 1.0$). Truncation of hexagons introduces pores or "empty tilings" to the hexagonal structure. Elongation of hexagons leads to a random tiling ($\zeta = 0.0$), compressed ($\zeta = 0.25$) and elongated ($\zeta = 0.75$ and 1.0) hexagonal (6^6) Archimedean tilings. (d) Pinched heptagons self-assemble into a disorder structure ($\xi = 0.0$), a dodecagonal quasicrystal ($\xi = 0.25$), a frustrated structure ($\xi = 0.5$), an ($3^2.4.3.4$) Archimedean tiling ($\xi = 0.75$) and a frustrated structure ($\xi = 1.0$). Truncated heptagons stabilize dodecagonal quasicrystals ($\gamma = 0.25$ and 0.5) and center rectangular tilings ($\gamma \geq 0.75$).

31

32